CrossMark

J. Fluid Mech. (2021), *vol*. 911, A19, doi:10.1017/jfm.2020.1047

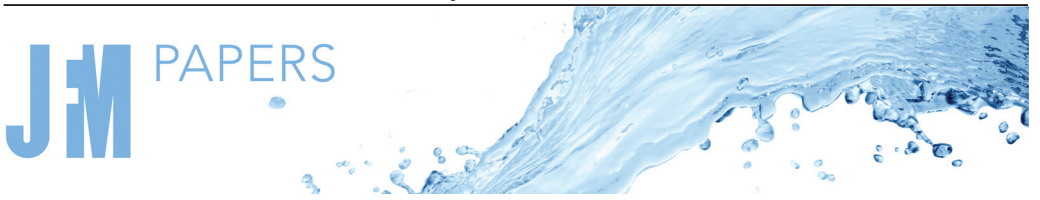

Two-dimensional oscillation of convection roll in a finite liquid metal layer under a horizontal magnetic field

Y. Tasaka[1,†], T. Yanagisawa[1,2], K. Fujita[1], T. Miyagoshi[2] and A. Sakuraba[3]

[1]Laboratory for Flow Control, Faculty of Engineering, Hokkaido University, Sapporo 060-8628, Japan

[2]Japan Agency for Marine–Earth Science and Technology (JAMSTEC), Yokosuka 237-0061, Japan

[3]Department of Earth and Planetary Science, University of Tokyo, Tokyo 113-0033, Japan

(Received 2 June 2020; revised 17 November 2020; accepted 18 November 2020)

We investigate the two-dimensional (2-D) oscillation of quasi-2-D convection rolls in a liquid metal layer confined by a vessel of aspect ratio five with an imposed horizontal magnetic field. Laboratory experiments were performed in the range of Rayleigh Ra and Chandrasekhar Q numbers of $7.9 \times 10^4 \leq Ra \leq 1.8 \times 10^5$ and $2.5 \times 10^4 \leq Q \leq 1.9 \times 10^5$ by decreasing Q at set Ra-number intervals to elucidate the features and mechanisms of oscillatory convection. Ultrasonic velocity profile measurements and supplemental numerical simulations show that the 2-D oscillations are caused by oscillations of recirculation vortex pairs between the main rolls, which are intensified by periodic vorticity entrainment from the vortex pair by the main rolls. The investigations also suggest that the oscillations occur at sufficiently large Reynolds Re numbers to induce instabilities on the vortex pair. The Re number is smaller for larger Q/Ra in the 2-D oscillation regime and the variations can be approximated by the effective Ra number; namely, the value reduced by the critical value for the onset of convection depending on Q. The variations steepen with further large Q/Ra and approach a scaling law of the velocity reduction as $(Ra/Q)^{1/2}$, which is established assuming that viscous dissipation is dominated by Hartmann braking at the walls perpendicular to the magnetic field. The results suggest that these phenomena are organized by the relationship between buoyancy and magnetic damping due to Hartmann braking.

Key words: Bénard convection, magneto convection, absolute/convective instability

† Email address for correspondence: tasaka@eng.hokudai.ac.jp

© The Author(s), 2021. Published by Cambridge University Press

https://doi.org/10.1017/jfm.2020.1047 Published online by Cambridge University Press

1. Introduction

Rayleigh–Bénard convection (RBC) refers to natural convection in a horizontal fluid layer caused by unstable vertical temperature stratification and is a fundamental flow system that creates large-scale fluid motion in both nature and industry. Convection is dominated by two dimensionless numbers, the Rayleigh number, $Ra = g\beta\Delta TL^3/(\kappa\nu)$, and the Prandtl number, $Pr = \nu/\kappa$, and the shape and size of the fluid layer, where g, ΔT and L denote the acceleration due to gravity, vertical temperature difference and height of the fluid layers, respectively, and β, κ and ν are the thermal expansion rate, thermal diffusivity and kinematic viscosity of the test fluids, respectively (see review papers and books by Koschmieder (1993), Bodenschatz, Pesch & Ahlers (2000), Ahlers, Grossmann & Lohse (2009), Lappa (2010) and Lohse & Xia (2010)). According to linear stability theory, the onset of convection in infinite fluid layers is independent of Pr, whereas the development of convective motion with increasing Ra number strongly depends on the Pr number. For Pr numbers smaller than unity, the transition from steady convection to thermal turbulence occurs more drastically with decreasing Pr number (Krishnamurti & Howard 1981). Such drastic transitions have also been represented by smaller stable regions of two-dimensional (2-D) convection rolls at smaller Pr numbers formed at the onset of convection. The stable region determined by stability analysis, the so-called 'Busse balloon', shrinks with decreasing Pr number (Busse 1978).

In actual situations of liquid metal layers ($Pr = O(10^{-2})$), the stable region of 2-D convection rolls can be difficult to access in experiments because of the very small cross-section of the Busse balloon at low Pr conditions. The application of a horizontal magnetic field enlarges the stable region and the quasi-2-D constraint arises from the influence of the Lorentz force with respect to the roll orientation. This reorganizes the flow structure in ways that ensure that both the global Joule dissipation and global kinetic energy decline in strict accordance with the conservation of linear and angular momentum (Davidson 1995). RBC affected by external magnetic fields is also characterized by the Chandrasekhar number, $Q = B^2L^2\sigma/(\rho\nu)$, which is the ratio of the Lorenz and viscous damping forces (equivalent to the square of the Hartmann number, $Q = Ha^2$), where B, σ and ρ denote the intensity of the external magnetic field, electrical conductivity and density of the test fluids, respectively. Linear stability theory suggests that the application of a horizontal magnetic field to infinite fluid layers does not affect the critical Ra value for the onset of convection (Chandrasekhar 1961), and weakly nonlinear theory (Clever & Busse 1987) predicts that magnetic fields with a small Q (e.g. $Q = 30$ for RBC in infinite fluid layers) widen the Busse balloon. One of the balloon boundaries is for the oscillatory instability that accompanies travelling waves on 2-D convection rolls. Further increases of Q on the applied magnetic field are expected to further widen the balloon, and oscillatory convection rolls with travelling waves would be observed even under relatively high Ra conditions. However, actual situations in finite fluid layers show different aspects, which are detailed below.

In the case of fluid layers confined by sidewalls (so-called finite fluid layers), the magnetic field restricts convection because of sidewall Hartmann braking, depending on the wall material. Burr & Müller (2002) expressed the effect as an upward shift of the neutral stability curve for the onset of convection, and predicted an increasing wavenumber of 2-D rolls with increasing Q. From laboratory experiments using eutectic sodium–potassium, $Na^{22}K^{78}$, Burr & Müller (2002) also reported the development of thermal turbulence via oscillatory convection by modifying the Ra and Q; thermal

https://doi.org/10.1017/jfm.2020.1047 Published online by Cambridge University Press

turbulence is suppressed with increasing Q for fixed Ra as variations of the power spectrum of the temperature fluctuations inside the fluid layer. However, the displayed variations do not present a straightforward progression to thermal turbulence, which leaves the detailed flow structure during these changes unexplained owing to a lack of flow field information.

Liquid metal experiments restrict the adoption of ordinary optical visualization techniques to observe flow fields because of their opaqueness. Recent developments in ultrasonic velocity profiling (or ultrasonic Doppler velocimetry using different terminology) (Eckert, Cramer & Gerbeth 2007; Takeda 2012) have provided a breakthrough in the understanding of this problem. Line measurements of instantaneous, single-velocity components in UVP provide both flow pattern and quantitative information of the spatio-temporal velocity field in liquid metal layers. As a typical example of UVP applied to RBC, small-scale turbulent statistics (Mashiko *et al.* 2004) and the behaviour of large-scale circulation (Tsuji *et al.* 2005) have been investigated. Quasi-2-D convection rolls in liquid metal layers confined by a rectangular vessel and periodic oscillatory motion of the rolls have also been visualized (Yanagisawa *et al.* 2010).

In our studies on RBC in a finite liquid metal layer confined by a horizontal magnetic field (Yanagisawa *et al.* 2013), we provided a regime diagram describing the development of the convection pattern from weak convection (very slow flows that are difficult to measure), steady quasi-2-D rolls, oscillatory convection and transition regimes to thermal turbulence with respect to Ra at fixed regions of somewhat small Q. In the regime diagram, the transitions between regimes are organized by Ra/Q. This relation holds over a widened regime diagram (Tasaka *et al.* 2016) at a somewhat higher Q range. The regime diagrams (Yanagisawa *et al.* 2013; Tasaka *et al.* 2016; Vogt *et al.* 2018) also indicate that a larger Q range generates smaller convection rolls (i.e. larger wavenumber of the structure), as predicted by Burr & Müller (2002). Vogt *et al.* (2018) recently investigated the development of convection flow structures with increasing Ra at fixed Q conditions to observe stepwise increases in Ra/Q. They reported that oscillatory convection occurs when maintaining the quasi-2-D state, which differs from the three-dimensional (3-D) travelling waves considered in the Busse balloon. Incipient instabilities can be assumed to be associated with quasi-2-D flow structures, and the 2-D character is lost with further reduction of the magnetic field until the flow ultimately becomes 3-D. Here, 2-D implies that the magnetic field reduces the velocity gradients along the magnetic field lines.

In this paper, we elucidate the 2-D oscillation features of convection rolls and their associated mechanisms, which disagree with theoretical predictions of a simple enlargement of the Busse balloon. This allows the present study to provide ideas for the Busse balloon when extended to the case of an applied horizontal magnetic field with vessel sidewalls. We investigated flow development with decreasing Q from sufficiently large values that forms steady convection at fixed Ra. This provides a simpler way to modify flow conditions than adjustments to Ra by simultaneously measuring both the flow field and temperature fluctuation using UVP and thermocouples. The spatio-temporal velocity field measurements allow monitoring of the variations in the number of rolls and also provide data for consideration from the point of view of specific velocity variations as they develop. After a brief description of the experimental arrangement, we detail the measurement tools and conditions in § 2. The experimental results and investigations on the morphology of the 2-D oscillations are summarized in § 3 with supplemental numerical simulations to show the flow structure details. A detailed discussion of the results in § 4 elucidates the conditions for the onset of oscillations with variations in the Reynolds number (Re) as inertia-induced oscillation.

https://doi.org/10.1017/jfm.2020.1047 Published online by Cambridge University Press

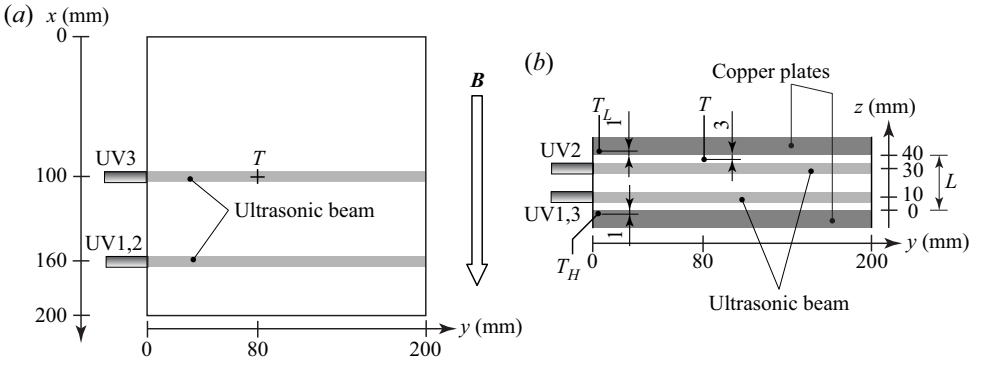

Figure 1. Experimental set-up, dimensions and sensor arrangement: (*a*) top view and (*b*) side view.

Physical properties	Symbol	Unit	Values
Thermal expansion coefficient	β	K^{-1}	1.24×10^{-4}
Thermal diffusivity	κ	$m^2\,s^{-1}$	1.05×10^{-5}
Kinematic viscosity	ν	$m^2\,s^{-1}$	3.31×10^{-7}
Density	ρ	$kg\,m^{-3}$	6.35×10^{3}
Electrical conductivity	σ	$(\Omega\,m)^{-1}$	3.26×10^{6}
Prandtl number	Pr	—	0.03
Magnetic Prandtl number	Pm	—	1.36×10^{-6}

Table 1. Physical properties of the test fluid, eutectic GaInSn ($Ga^{67}In^{20.5}Sn^{12.5}$) at 25 °C (Morley *et al.* 2008; Plevachuk *et al.* 2014).

2. Experimental set-up and measurement procedure

The experimental arrangement used here has also been applied in a series of previous studies (Yanagisawa *et al.* 2011, 2013; Tasaka *et al.* 2016; Vogt *et al.* 2018). The vessel has a square cross-section with 200 mm sides and $L = 40$ mm height, as shown in figure 1. The vessel is bounded by copper plates at the top and bottom to achieve isothermal boundaries and by resin walls at the sides to ensure thermal and electrical insulation. Channels machined in the top and bottom copper plates were connected to thermostatic baths and water circulation maintained a constant temperature at the top and bottom vessel boundaries. The test fluid for the fluid layer filling the vessel is eutectic gallium–indium–tin ($Ga^{67}In^{20.5}Sn^{12.5}$), which is electrically conductive and has a small Prandtl number ($Pr \sim 0.03$). Details of the material properties are summarized in table 1. A quasi-uniform magnetic field ($\boldsymbol{B}$ in figure 1) was created using an electromagnet consisting of two water-cooled copper coils and a magnetic yoke. The maximum intensity and non-uniform magnetic field strength were 700 mT and better than 7 % at maximum intensity.

Two measurement techniques were used in the experiments, ultrasonic velocity profiling (UVP) and thermocouples for capturing the flow field and temperature fluctuations, respectively. Sensor arrangements are shown in figure 1 from a top view (*a*) and side view (*b*). Three ultrasonic transducers for the UVP were mounted on the vessel: at $z = 10$ mm from the bottom plate and 40 mm from the sidewall ($x = 160$ mm) for UV1; $z = 30$ mm and $x = 160$ mm for UV2; and $z = 10$ mm and $x = 100$ mm for UV3. The instantaneous flow velocity profiles were recorded along the propagation lines of the ultrasonic waves,

https://doi.org/10.1017/jfm.2020.1047 Published online by Cambridge University Press

$u_y(y, t)$, which were aligned perpendicular to the magnetic field. One thermocouple (T) was placed in the fluid layer (figure 1), 3 mm below the top plate. Two thermocouples were inserted in the top and bottom copper plates to monitor the temperature at the vessel boundaries, top, T_L and bottom, T_H. The temperature difference used to calculate Ra is obtained as $\Delta T = T_H - T_L$. Details of the experimental set-up are also provided in Tasaka *et al.* (2016).

The experiments were strictly carried out according to the following procedure. The temperature difference was first adjusted by controlling the temperatures in the thermostatic baths. After 30 min, a magnetic field was applied. After an additional 10 min, the flow measurements began, assuming that the fluid layer had reached equilibrium. In each series of experiments, which were always started at the highest magnetic field strength, the temperature difference was held constant and the magnetic field intensity was reduced in stages. At each stage, the field intensity was held constant for 30 min, which is considerably longer than the thermal diffusion time of the fluid layer (153 s) and turnover time of a single convection roll (6–10 s). The total measurement time was longer than 4 h for the shortest experiments.

We performed direct numerical simulations for the same geometry as in the laboratory experiment, considering a horizontal magnetic field imposed on a rectangular vessel with no-slip velocity boundaries. The numerical code used here is identical to that in Yanagisawa, Hamano & Sakuraba (2015) and Vogt *et al.* (2018), and successfully reproduces the diverse convection regimes observed in the experiments for variations of Ra and Q. In the code, a set of governing equations for magnetohydrodynamic flows is solved for a Boussinesq fluid (see Yanagisawa *et al.* (2015) for further details). The Pr number for the simulations was set to 0.025. The grid resolution is a compromise between a sufficient number of grid points in the Hartmann layer and reasonable computation time. The calculations were conducted on a mesh of $600 \times 600 \times 120$ grid points. Additional calculations were performed at a finer mesh with $1280 \times 1280 \times 256$ grid points for shorter durations to check the reliability of the results.

3. Results

3.1. *Variety of initial number of rolls at high Q*

The application of a magnetic field restricts flow structures to quasi-2-D shape by Joule dissipation on the fluid motion parallel to the magnetic field (Davidson 1995). For RBC with a horizontal magnetic field, this provides convection rolls arranged parallel to the magnetic field, and also modifies the number of convection rolls (i.e. wavenumber of the structure) depending on Ra and Q (Yanagisawa *et al.* 2013; Tasaka *et al.* 2016). Unlike our earlier studies conducted at smaller Q (Yanagisawa *et al.* 2011, 2013; Tasaka *et al.* 2016), a notable feature of the present experiments performed at relatively high Q is that several repetitions of the experiments do not produce exactly the same number of convection rolls. Depending on the Ra number, different probabilities are found for the occurrence of an initial number of rolls n. Figures 2(*a*)–2(*f*) show histograms of the probability density on n observed at a fixed Q of 2.0×10^5, and variable Ra values (2.3×10^4 to 1.5×10^5), where solid circles with bars represent the averages and corresponding standard deviations. The number of rolls was identified using the spatio-temporal velocity maps, $u_y(y, t)$, measured by the ultrasonic transducer (UV1, figure 1). An example of a map is shown in figure 2(*g*), where the seven white and black stripes represent individual convection rolls and the adjacent rolls show opposite rotation directions. The identification of the number of rolls based on velocity measurements along the measurement line perpendicular to the magnetic

https://doi.org/10.1017/jfm.2020.1047 Published online by Cambridge University Press

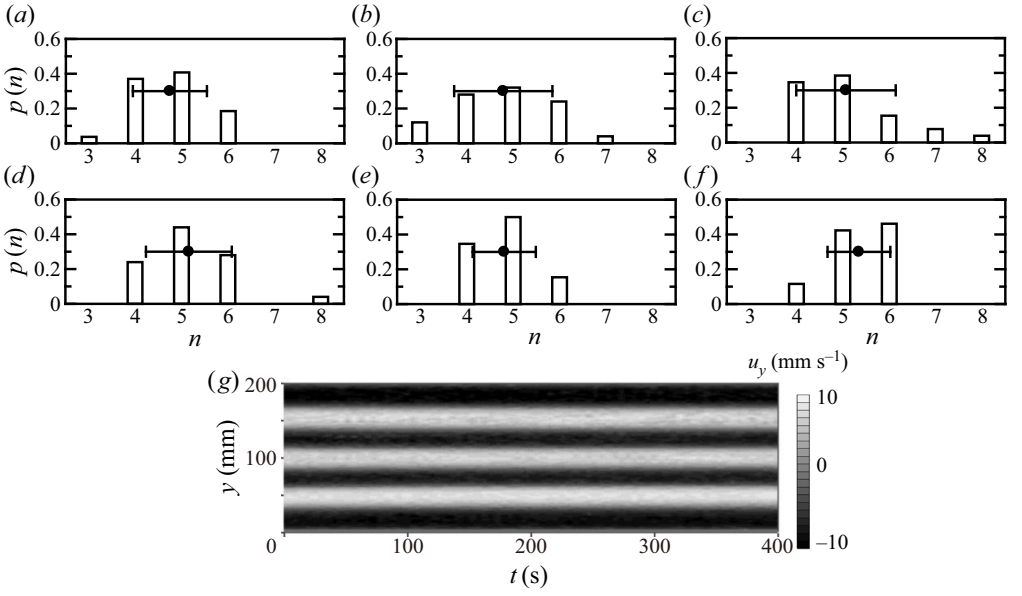

Figure 2. Probability density function for the initial number of convection rolls observed at $Q = 2.0 \times 10^5$ and at several Ra numbers: (*a*) 2.3×10^4, (*b*) 3.8×10^4, (*c*) 7.7×10^4, (*d*) 9.2×10^4, (*e*) 1.2×10^5, and (*f*) 1.5×10^5, where solid circles with bars represent the average and standard deviations. (*g*) An example of a spatio-temporal velocity map for $n = 7$.

field is quite straightforward, because a sufficiently high field strength stabilizes the rolls and aligns them along the field lines. The seven-roll regime ($n = 7$) shown in figure 2(*g*) was first observed in this study, whereas previous studies assumed this number of rolls for sufficiently high Q from the observation that n increases with Q (Yanagisawa *et al.* 2013; Tasaka *et al.* 2016).

The initial number of convection rolls obtained in the present experiments ranges from $n = 3$ to 8 as shown in the histograms (figure 2*a–f*). In these, $n = 3$, 4 and 8 are unstable states, where the initial roll number changed over time for the same Ra and Q numbers. With three stable states, $n = 5$, 6 and 7 occur with bistability that has not been previously reported for smaller Q. This may be due to a reduced horizontal size of the stable convection rolls at larger Q relative to the vessel size, $\Gamma = 5$ in aspect ratio. The experimental procedure in the present study, giving initially a certain temperature difference for the set Ra number, may also affect the bistability. The average and standard deviation of n in the histograms show no significant tendency with respect to Ra number in the range examined here.

The present study focuses on the onset of convection roll oscillations with decreasing Q at a given Ra number by velocity mapping and temperature fluctuation measurements. The thermocouple positions with respect to the convection rolls must be taken into account to evaluate the temperature fluctuation because, in the case of oscillations, their amplitude should be greater if the measuring position is in between two adjacent rolls. In the stable states, five- and six-roll states are sustained with decreasing Q whereas the seven-roll state shows a transition to the six-roll state with slight decrease of Q. We therefore investigated the onset of the oscillations for the five- and six-roll states. In figure 3, the examined Ra and Q values are displayed with the corresponding roll number state and flow regimes with different symbols. Light circular symbols with a central mark and bold circular

https://doi.org/10.1017/jfm.2020.1047 Published online by Cambridge University Press

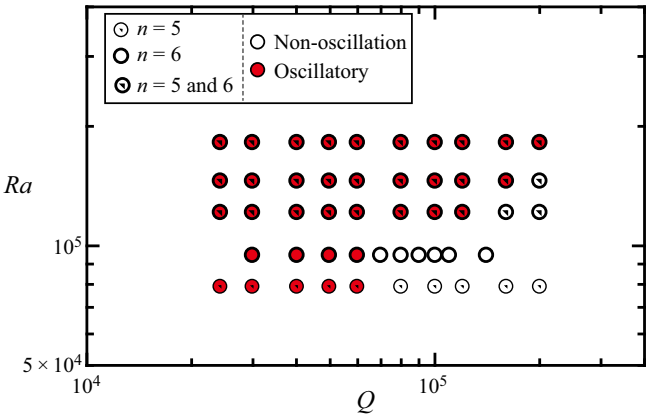

Figure 3. Parameter range examined in the present experiments. Open and red-filled circles represent non-oscillation and oscillatory states, respectively. The thickness of the circle and central mark in the circles indicates the corresponding number of rolls.

symbols with no central mark indicate five- and six-roll states, respectively, and bold circular symbols with a central mark indicate that both states are observed for the same set parameters; and open and red-filled symbols represent non-oscillation and oscillatory regimes, respectively. The recognition of an oscillatory or non-oscillation regime was tentatively given from the spatio-temporal velocity map.

3.2. *Onset of oscillatory convection*

Each measurement series performed for a Ra number starts with sufficiently large Q values at which distinct oscillatory motion is not observed. With the stepwise reduction of the magnetic field, oscillations occur at certain Q, whose properties change with further reduction of Q. Figure 4 shows an example for an oscillating five-roll state at $Ra = 1.2 \times 10^5$ and $Q = 5.0 \times 10^4$. The spatio-temporal velocity map in figure 4(*a*) was measured by UV1 and the corresponding temperature fluctuation in figure 4(*b*) was measured by the temperature probe T (figure 1). In the velocity map, oscillations are visible as periodic changes in the boundaries between the neighbouring convection rolls, with the three inner rolls showing greater fluctuations than those on the vessel sidewalls. The main features are similar to those observed in the 2-D oscillations (Vogt *et al.* 2018, figures 4 and 10), which are the main subject for investigation in the present study. The two-dimensionality of the oscillations is further evaluated below. The corresponding temperature fluctuation shows clearer periodic oscillations than in the velocity map; in the five-roll state, the position of probe T is at the boundary between the second and third rolls and can effectively capture the oscillation because of the relatively large oscillation amplitude expected at the boundary.

The power spectra from a Fourier transformation of the fluctuations of velocity and temperature shown in figure 4 are plotted in figure 5. The velocity fluctuation for the spectra in figure 5(*a*) is extracted from figure 4(*a*) at $y = 120.56$ mm and corresponds to the boundary between the main convection rolls, where the root-mean-square (r.m.s.) value of the velocity fluctuations reaches the maximum. Both spectra have a sharp peak corresponding to the roll oscillation at $f = 0.086$ Hz (f_{OS}). The critical Chandrasekhar number for the onset of oscillations, Q_{OS}, is determined from the velocity fluctuations. Taking into account the occurrence of the five- or six-roll state, the location to extract the

https://doi.org/10.1017/jfm.2020.1047 Published online by Cambridge University Press

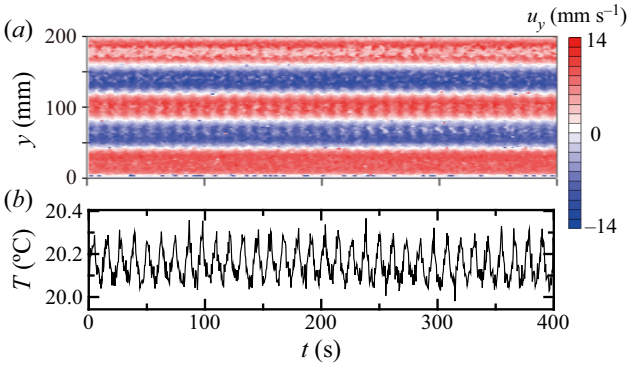

Figure 4. Sample of (*a*) spatio-temporal velocity map measured by UV1 and (*b*) corresponding temperature fluctuations measured by temperature probe T (figure 1) in the oscillation regime at $Ra = 1.2 \times 10^5$ and $Q = 5.0 \times 10^4$.

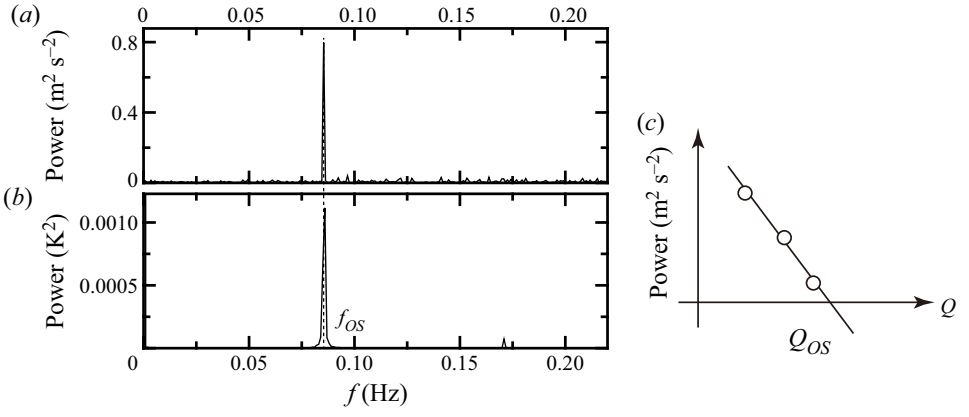

Figure 5. Power spectra for (*a*) velocity (at $y = 120.56$ mm) and (*b*) temperature fluctuations, both with the data shown in figure 4. (*c*) Schematic diagram for the variation of peak power of the frequency component of the velocity fluctuation at $f = f_{OS}$.

velocity fluctuations is always chosen as the boundary between the two central convection rolls. The zero-crossing point from the linear extrapolation of the spectral peak values from the velocity fluctuations gives the critical value Q_{OS} (see schematic diagram in figure 5*c*). The spectral peak values of the temperature fluctuations are also used to cross-check the Q_{OS} values estimated from the velocity fluctuations.

The determined Q_{OS} values obtained at both the five- and six-roll states and at different Ra numbers are plotted in figure 6, with the five- and six-roll states shown by solid squares and open circles, respectively. The symbols for the two states appear to overlap, which suggests only a small influence of the number of rolls on the onset of oscillation. For comparison, the critical values obtained in similar experimental work by Burr & Müller (2002) are plotted as crosses in figure 6. The difference between the present results and data obtained in Burr & Müller (2002) is apparent, even if different criteria and procedures were applied to determine the critical values. For a given Q value, the critical Ra number for the onset of oscillatory convection is one order of magnitude smaller than the present results. The most significant difference between the experiments is the size of the fluid layer; the present study uses a square vessel with $\Gamma = 5$ aspect ratio, whereas Burr &

https://doi.org/10.1017/jfm.2020.1047 Published online by Cambridge University Press

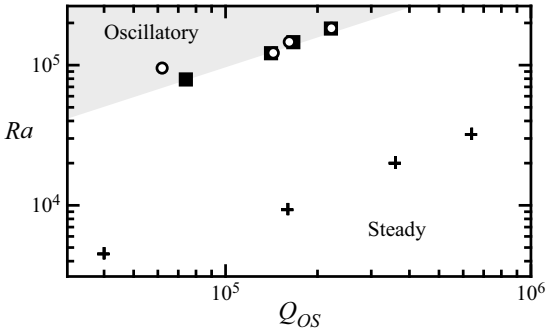

Figure 6. Critical Q for the onset of oscillation, Q_{OS}, obtained at different Ra values with decreasing Q. Solid squares and open circles represent Q_{OS} for $n = 5$ and 6, respectively. The crosses indicate critical Ra numbers for the onset of oscillation obtained at different Q values from Burr & Müller (2002).

Müller (2002) used a larger rectangular vessel with sides of $10L$ and $20L$ in directions, respectively, parallel and perpendicular to the magnetic field. Simply stated, this difference is from a magnetohydrodynamics (MHD) effect due to the vessel size and differences in the oscillatory convection criteria. A detailed investigation of the corresponding flow structures in § 3.4 elucidates that a different oscillatory convection type emerges even below the boundary determined here. These points are further discussed below.

3.3. *Development of oscillatory convection*

This section considers the development of oscillation intensity with decreasing magnetic field strength beyond the onset of oscillations at $Q = Q_{OS}(Ra)$. Temperature fluctuations are used to monitor the development instead of the spatio-temporal velocity maps. This decision is justified by the long measurement times of approximately 4 h, during which a noticeable separation of reflecting particles occurs due to the small difference in density between the liquid metal and particle. This leads to a deterioration of the measured signals by the increasing noise level. The variations of r.m.s. of the temperature fluctuations, T_{rms}, with decreasing Q are shown in figure 7(*a*) for different Ra values, in a five-roll state (i.e. $n = 5$). The grey band at the bottom of the figure indicates the noise level below which no temperature fluctuations can be reliably detected. The points at which the curves reach the noise level correspond fairly well with the onset of oscillations determined by analysing the velocity data (see figure 5).

The variations of T_{rms} versus Q can be merged into a single curve by normalizing T_{rms} with the maximum r.m.s. value, $T_{rms,max}$, for the respective measurement series at a given Ra (figure 7*b*) and Q with Ra values. This suggests that developments in the oscillation are organized by Ra/Q, such as the organization of different flow regimes determined in our previous studies (Yanagisawa *et al.* 2013; Tasaka *et al.* 2016; Vogt *et al.* 2018). It may be expected from the unified curves that T_{rms} decreases with a further reduction of Q at lower Ra conditions than $Ra = 1.8 \times 10^5$. This might be caused by 3-D developments of the oscillatory motion of a convection roll (Vogt *et al.* 2018), and is discussed further in § 3.5 from the viewpoint of the oscillation frequency and characteristic velocity of the convection roll.

3.4. *Structures and source of the 2-D oscillations*

To verify the two-dimensionality of the oscillatory motions from phase differences of the local velocity fluctuations, we simultaneously measured velocity profiles along three

https://doi.org/10.1017/jfm.2020.1047 Published online by Cambridge University Press

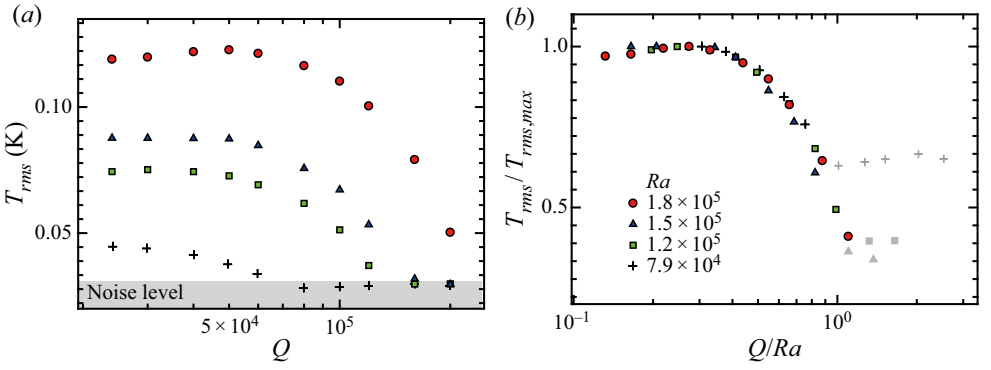

Figure 7. (*a*) Variations of the r.m.s. value of the temperature fluctuations T (figure 1) with decreasing Q at different Ra values, where the grey hatched area represents data lower than the noise level. (*b*) Variations normalized by the maximum r.m.s. values, with respect to Q/Ra, where the grey symbols (right side) represent data points lower than the noise level. The corresponding number of convection rolls is $n = 5$ (five-roll state).

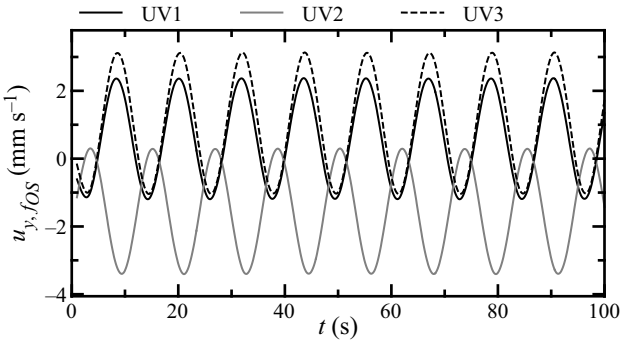

Figure 8. Velocity fluctuations extracted at $f = f_{OS}$ by Fourier transformation from the original velocity fluctuations measured by different ultrasonic transducers, UV1 to UV3 (figure 1) at $y = 120.56$ mm, and at $Ra = 1.2 \times 10^5$ and $Q = 5.0 \times 10^4$.

different measurement lines at UV1, UV2 and UV3 (figure 1). The velocity fluctuations corresponding to $f = f_{OS}$ were extracted by discrete Fourier transformation from the time series of the velocity signals for the position $y = 120.56$ mm, where two neighbouring rolls encounter each other. Figure 8 presents the velocity time series of all three sensors, showing distinct oscillations at $f = f_{OS}$. The signals of sensors UV1 and UV3, which are mounted at the same height ($z = 10$ mm) and different x-positions ($x = 160$ and 100 mm), are in phase, whereas the signals recorded by UV1 and UV2 mounted at the same x-position at the bottom ($z = 10$ mm) and top ($z = 30$ mm) of the fluid layer oscillate in antiphase. These results coincide with the basic features of the 2-D flow structure and thus fundamentally differ from the 3-D travelling wave oscillations in conventional Rayleigh–Bénard convection (Clever & Busse 1987).

The reason that 2-D oscillatory motion appears at the onset of oscillatory convection rather than the 3-D travelling waves, as predicted in previous studies (Busse & Clever 1983; Clever & Busse 1987), requires further explanation. Stability analysis performed by Busse & Clever (1983) indicated that the stable region boundary of the 2-D convection rolls in ordinarily occurring oscillatory instability widens by applying a horizontal magnetic field. Our measurements suggest that another type of instability occurs in the

https://doi.org/10.1017/jfm.2020.1047 Published online by Cambridge University Press

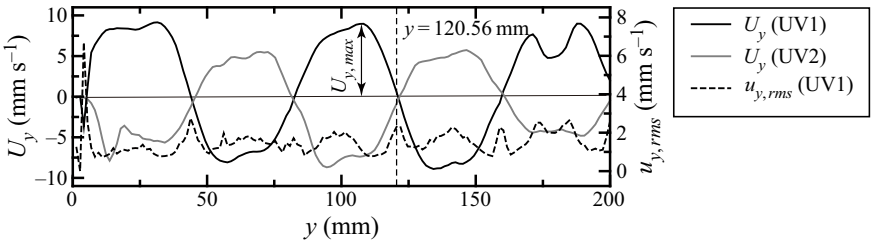

Figure 9. Profiles of mean velocity U_y and standard deviation of velocity fluctuations $u_{y,rms}$ measured at $Ra = 1.2 \times 10^5$ and $Q = 5.0 \times 10^4$ ($Q/Ra = 0.42$) by ultrasonic transducers at the bottom and top positions, UV1 and UV2 (figure 1) (the corresponding spatio-temporal velocity map for UV1 is shown in figure 4*a*).

case of the magnetic field. This section discusses the mechanics of these 2-D oscillations, together with the details of roll motion corresponding to the 2-D oscillations obtained in the present experimental results.

The mean flow structure in the case where the 2-D oscillations occur at $Ra = 1.2 \times 10^5$ and $Q = 5.0 \times 10^4$ ($Q/Ra = 0.42$) is presented in figure 9 as profiles of the time-averaged velocity U_y (solid line) measured at the bottom (black, UV1) and top (grey, UV2) (see figure 1). The mean velocity profile exhibits five conversions of flow directions corresponding to a five-roll state. However, the profile shape is not simply sinusoidal but shows substantial asymmetric deformations (i.e. humps). Furthermore, neighbouring positive and negative parts of the profile with a hump seem to appear in the point symmetry, and the profiles measured by the top and bottom line are also related by point symmetry. A profile of the standard deviation of the velocity fluctuations measured along the bottom line (UV1), $u_{y,rms}$, is also plotted in figure 9 (broken line). The standard deviation assumes sharp peaks around positions with $U_y = 0$, corresponding to the boundaries between rolls and large values around the deformation area of the U_y profiles.

We performed additional numerical simulations to obtain more details of the structures corresponding to the typical velocity profiles. The simulation parameters were set close to the experimental conditions in figure 9, $Ra = 1.0 \times 10^5$ and $Q = 3.2 \times 10^4$ ($Q/Ra = 0.32$). The isosurface of the Q_{3D} value, the second invariant of the velocity gradient tensor calculated from the simulation results, displays convection rolls. A quasi-2-D shape of the rolls in the oscillatory condition provides evidence of 2-D oscillatory motion (figure 10*a*). We also calculated a spatio-temporal velocity map from the simulation results along a line corresponding to the present UV1 line measurement ($z = 0.25L$; dark red line in figure 10*a*). This map shows finer structures of the oscillatory convections (figure 10*b*). The corresponding mean velocity profile shown in figure 10(*c*) also has humps that reflect modifications of the main rolls. Figures 10(*d*)–10(*f*) show sequential snapshots of the vorticity field on a vertical cross-section of the fluid layer perpendicular to the magnetic field (ω_x). Red and blue contours in the various panels represent positive and negative values of vorticity in the direction of the applied magnetic field (x-axis), respectively. The broken line in figure 10(*d*) indicates the measurement line corresponding to the ultrasonic transducer (figure 1). At the places corresponding to the humps, there is an additional recirculation vortex pair between the main rolls. The vortices seem to be a separation vortex pair from the main rolls and appear in between the roll flows detached from the wall, not approaching or adhering to the wall.

Sequential snapshots shown in figure 10(*d–f*) also represent the motion of the rolls corresponding to the 2-D oscillations as a periodic distortion of the rolls into elliptic shapes. A remarkable feature of this distortion is that the roll axes are almost fixed

https://doi.org/10.1017/jfm.2020.1047 Published online by Cambridge University Press

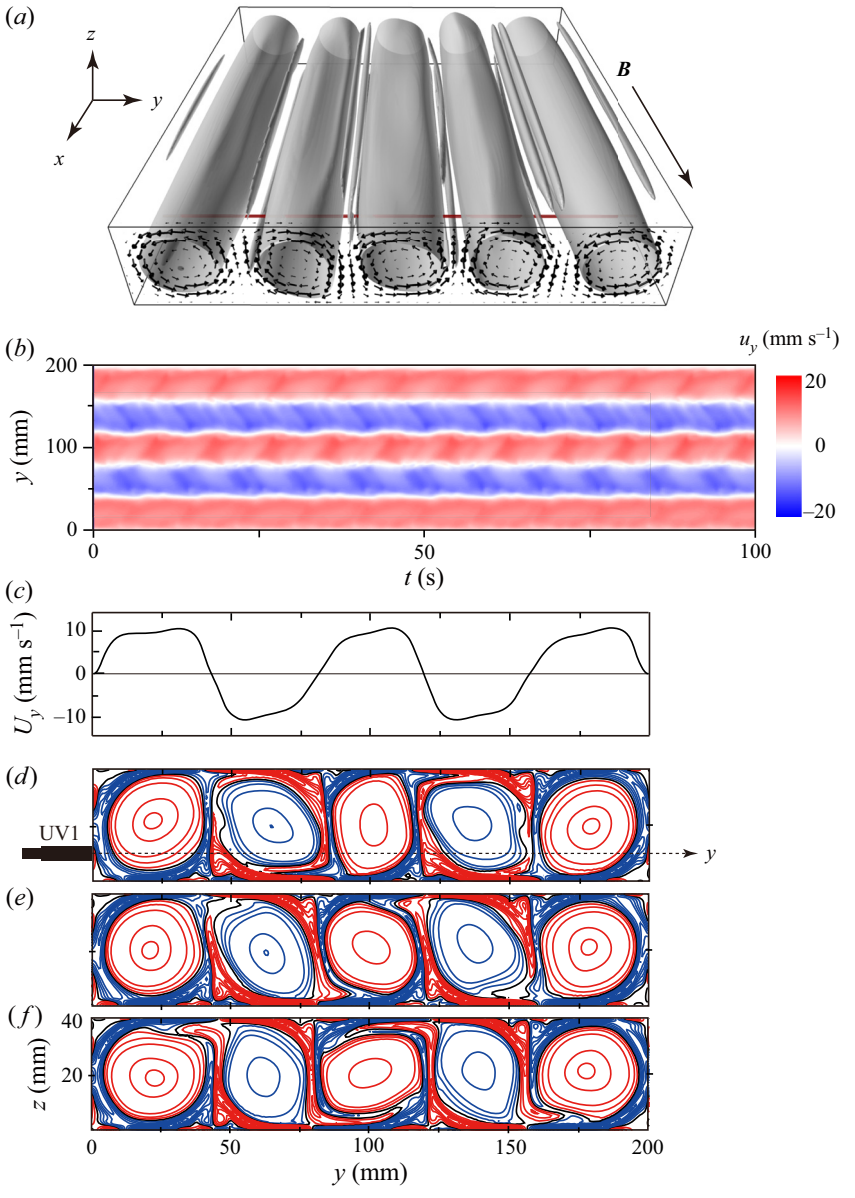

Figure 10. Results of numerical simulation performed for $Ra = 1.0 \times 10^5$ and $Q = 3.2 \times 10^4$ ($Q/Ra = 0.32$). (*a*) The isosurface of Q_{3D} represents the roll structures, where the dark red line indicates the place of the UV1 measurement line. (*b*) Spatio-temporal velocity map extracted along a line corresponding to the UV1 measurement line (see figure 1). (*c*) Time-averaged velocity profile of the velocity map. (*d–f*) Instantaneous contour maps of vorticity on the vertical cross-section at $x = 160$ mm, where red and blue contours represent positive and negative values of the vorticity, respectively (see also supplementary movie 1).

at both horizontal and vertical positions. The distortion is accompanied by entraining the vorticity from the recirculation vortex pair; the entrainment occurs periodically and alternately between neighbouring main rolls, and deformation of the rolls behaves synchronously (see also supplementary movie 1 available at https://doi.org/10.1017/jfm.2020.1047). By the entrainment, the main rolls seem to be surrounded by an annular layer

https://doi.org/10.1017/jfm.2020.1047 Published online by Cambridge University Press

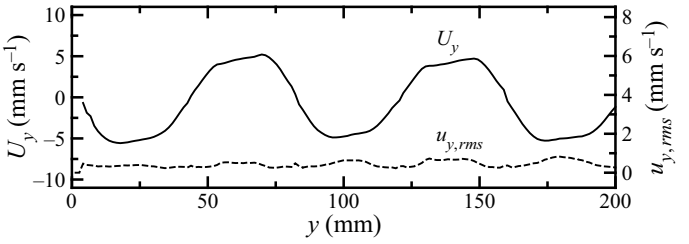

Figure 11. Profiles of mean velocity U_y and standard deviation of velocity fluctuations $u_{y,rms}$ measured at $Ra = 7.9 \times 10^4$ and $Q = 2.0 \times 10^5$ ($Q/Ra = 2.5$) by UV1.

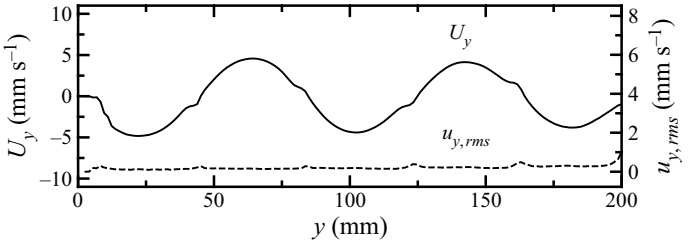

Figure 12. Profiles of mean velocity U_y and standard deviation of velocity fluctuations $u_{y,rms}$ using data from Vogt *et al.* (2018) at $Ra = 1.7 \times 10^4$ and $Q = 8.0 \times 10^3$ ($Q/Ra = 0.47$) by UV2.

of opposite-sign vorticity. In this oscillation mode, fluid particles may follow an elliptic particle path in a y–z cross-section different from the 3-D travelling wave oscillations. Along the periodic distortion, the cross-sectional area of the rolls periodically expands and shrinks similar to 'breathing'. This behaviour of the rolls with rotation of the major axis of the elliptic shape is expressed by diagonal lines on the space–time velocity map (figure 10*b*). Similar diagonal stripe patterns are also observed in the velocity map measured by UVP (figure 4*a*). This supports the reliability of this numerical simulation.

No oscillatory convection is detected at $Q > Q_{OS}(Ra)$, according to the present criteria. We investigated the mean velocity profile taken at this condition of the experiment to highlight the differences in the convection roll structures (figure 11). Here the profile was measured along UV1 at $Ra = 7.9 \times 10^4$ and $Q = 2.0 \times 10^5$ ($Q/Ra = 2.5$). The profile still has small but distinct humps and is asymmetric, representing elliptic main rolls with small recirculation vortex pairs. The corresponding r.m.s. values of the velocity fluctuations are small but significantly distributed. This condition therefore cannot be distinguished as a steady-state regime, even though a distinct peak frequency is not detected on the velocity fluctuation spectra. Under considerably smaller Ra conditions, the velocity profile assumes a sinusoidal shape with horizontal symmetry in each roll. An example of these profiles is shown in figure 12 as the mean velocity profiles, where the original velocity data for the profile is from Vogt *et al.* (2018) measured at $Ra = 1.7 \times 10^4$ and $Q = 8.0 \times 10^3$ ($Q/Ra = 0.47$) by UV2. Even in this condition, the profile of the r.m.s. value shows small, local maxima at the boundaries between the main rolls. A numerical simulation was also performed at similar parameters, $Ra = 1.4 \times 10^4$ and $Q = 5.7 \times 10^3$ ($Q/Ra = 0.41$), to determine the corresponding motion of the main rolls. A snapshot of the isosurface of the Q_{3D} value also represents quasi-2-D rolls along the direction of the magnetic field (figure 13*a*).

The spatio-temporal velocity map shown in figure 13(*b*) extracted from the simulation results along the line corresponding to the UV2 measurement line (dark red line in

https://doi.org/10.1017/jfm.2020.1047 Published online by Cambridge University Press

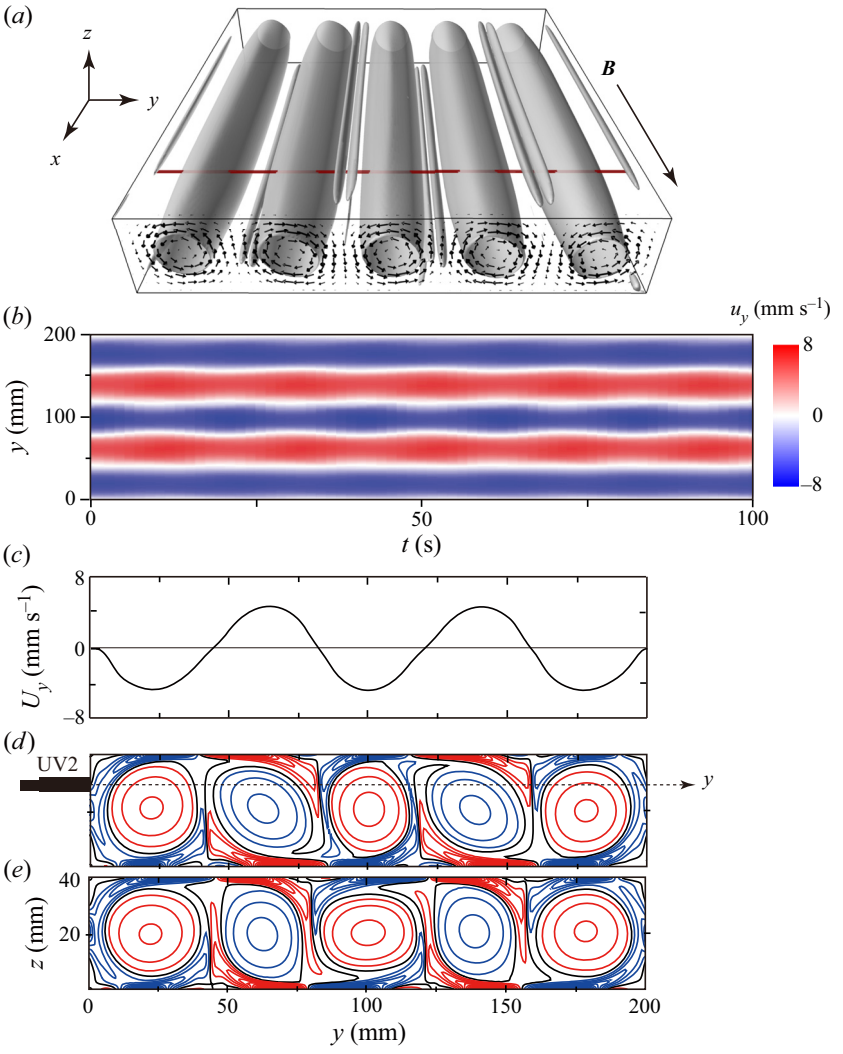

Figure 13. Results of numerical simulation performed for $Ra = 1.4 \times 10^4$ and $Q = 5.7 \times 10^3$ ($Q/Ra = 0.41$). (*a*) Isosurface of the Q_{3D} value representing roll structures, where the dark red line indicates the UV2 measurement line. (*b*) Spatio-temporal velocity map extracted along a line corresponding to the UV2 measurement line (figure 1). (*c*) Time-averaged velocity profile of the velocity map. (*d*,*e*) Instantaneous contour map of vorticity on the vertical cross-section at $x = 160$ mm, where red and blue contours represent positive and negative values of the vorticity, respectively (see also supplementary movie 2).

figure 13*a*) displays longer-period periodic oscillation with substantially smaller amplitude than in the oscillations shown in figure 10(*b*). The mean velocity profile calculated from the map also has a quasi-sinusoidal shape with small deformation around the boundaries between the main rolls (figure 13*c*). Contour maps of the instantaneous vorticity field given from the simulation show the existence of small recirculation vortex pairs (figures 13*d* and 13*e*; see also supplementary movie 2). The numerical simulation elucidates that the vortex pair oscillates periodically and locally, and the distinct peaks of the r.m.s. values shown in figure 12 may represent such local oscillations. Such small vortex pairs and oscillations may not be distinguished by UVP measurements in the present experiment

https://doi.org/10.1017/jfm.2020.1047 Published online by Cambridge University Press

because of the arrangement of the measurement lines relative to the vortex pair and the inability to resolve small velocity fluctuations. The results summarized above suggest that there are two different types of 2-D oscillatory convection: weak and local oscillations on the recirculation vortex pair (corresponding to figures 11–13), and more dynamic and global elliptic oscillations of the main rolls accompanied by vorticity entrainment from the recirculation vortex pairs (figures 9 and 10).

Previous studies that assumed a wake of straight cylinders reported that such recirculation vortex pairs show absolute instability at relatively small Reynolds numbers, $Re = O(10)$, and display periodic oscillations (e.g. Drazin & Reid 1998). With increasing Re number, $O(10^2)$, the oscillations propagate from the recirculation vortex pair downstream. Here, unlike the wake, the main rolls are in tight interaction with the recirculation vortex pairs via vorticity entrainment and elliptic deformation of the roll in the 2-D oscillation with increasing velocity of the main rolls. In the next section, we investigate the convective flow velocity and dimensionless frequency of the oscillatory motion to characterize the 2-D oscillations.

3.5. *Frequency and flow velocity on the 2-D oscillatory convection*

This section discusses the characteristic frequency of the oscillatory convection f_{OS} and the local maximum value of the time-averaged velocity profile at the central convection rolls $U_{y,max}$ (figure 9), which are the basis for calculating the dimensionless frequency and Re numbers. Variations in these values with respect to Q are shown in figure 14. The f_{OS} and $U_{y,max}$ values for the plots were obtained from spatio-temporal velocity maps measured by UV1 at different Ra numbers for the five-roll state via the spatially averaged power spectrum of the velocity fluctuations and time-averaged velocity profile, respectively. The f_{OS} detected by UV3 placed at the centre of the vessel parallel to UV1 are also plotted to evaluate the range of the 2-D oscillations in figure 14(*a*). The frequency gradually increases with decreasing Q at all of the Ra conditions studied here, with the largest increases observed for small Q and the highest Ra number of $Ra = 1.8 \times 10^5$. There is a very close coincidence of the f_{OS} obtained by UV1 and UV3 at relatively large Q values within the frequency resolution as expressed by the symbol overlap. At smaller Q, however, distinct peaks corresponding to f_{OS} in UV3 cannot be distinguished and are buried in multiple peaks or noise, whereas the spectra obtained by UV1 show clear peaks. The coincidence suggests the existence of 2-D oscillations, whereas the disappearance may indicate a transition from the 2-D oscillatory convection regime to a 3-D flow regime. Vogt *et al.* (2018) suggested that a transition from quasi-2-D convection to a 3-D flow regime appears as a meandering structure along the centreline of the vessel perpendicular to the magnetic field while fine structures move along the roll axis. The disappearance of a distinct peak in the spectra obtained by UV3 may reflect this; however, further detailed investigation is beyond the scope of the present study.

The dependence of U_y on Q shown in figure 14(*b*) is similar to the behaviour of the temperature oscillations in figure 7(*a*): the mean velocity initially slightly increases with decreasing magnetic field, reaches a maximum and then decreases. These observations can also be understood as growth of the 2-D oscillations and subsequent transition to a 3-D flow regime. At the opposite viewpoint, $U_{y,max}$ increases with increasing magnetic field strength in the range of small Q. This effect can likely be attributed to the stabilization and strengthening of the mean flow by the magnetic field. Burr & Müller (2002) reported an increase in heat transfer in RBC with the application of a horizontal magnetic field over a specific parameter range for Hartmann numbers $Ha = Q^{1/2} < 400$. As an explanation

https://doi.org/10.1017/jfm.2020.1047 Published online by Cambridge University Press

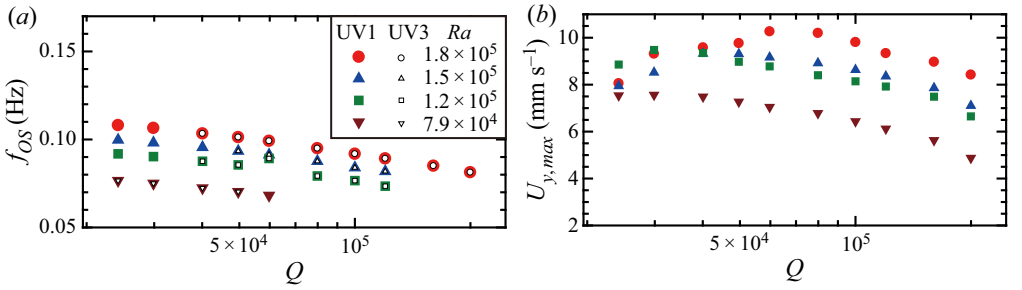

Figure 14. Variations of (*a*) the main frequency on the oscillatory convection, f_{OS}, obtained by UV1 and UV3, and (*b*) the maximum time-averaged velocity of the central convection rolls, $U_{y,max}$, in the five-roll state with respect to Q obtained at different Ra. In (*a*), the frequencies obtained by UV3 at most of the Q values agree with those by UV1 within the frequency resolution as overlaps of the solid and open symbols.

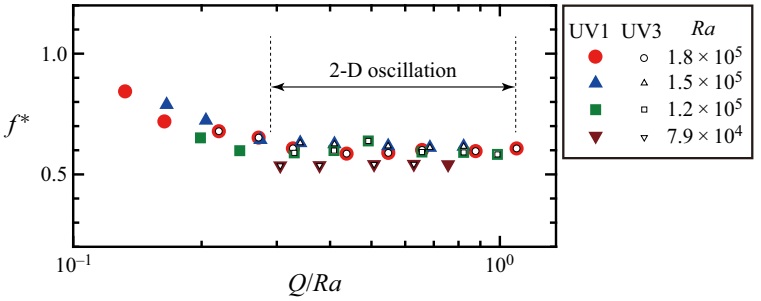

Figure 15. Dimensionless frequencies determined by UV1 and UV3 plotted at different Ra versus Q/Ra, where the frequencies obtained by UV3 at most of the Q/Ra values agree with those by UV1 within the frequency resolution as overlaps of the solid and open symbols. There exist no symbols for UV3 for small Q/Ra values because of unclear frequencies by UV3.

for the increase of flow transport properties, the authors suggested an enhancement of the quasi-2-D roll-type convection. A damping of the flow intensity occurs with further increases in Q due to the emerging magnetic damping. This point is important in the discussion of flow transition and is further addressed in the following section.

The dimensionless frequency reduced by the circulation time (turnover time) of the main convection rolls, $f^* = f_{OS}\tau_{TO}$, is plotted as a function of Q/Ra in figure 15, where the circulation time is given as $\tau_{TO} = 2\pi\Delta z/U_{y,max}$, with the displacement of the measurement line from the centre of the rolls, $\Delta z = 10$ mm (figure 1). At sufficiently high magnetic fields ($Q/Ra \gtrsim 0.3$) the values obtained by UV1 and UV3 collapse into a unified curve (i.e. the symbols overlap) and f^* assumes a nearly constant value around 0.6. The supplemental numerical simulations shown in figures 10 and 13 provide a similar dimensionless frequency, $f^* \sim 0.6$. As mentioned, the finding of a consistent and constant dimensionless frequency can be interpreted as an indication of a 2-D flow structure, whereas the scattering of the data for $Q/Ra \lesssim 0.3$ can be understood as the transition from the 2-D oscillatory convection regime to a 3-D flow regime. The transition point at $Q/Ra \approx 0.3$ corresponds to the one at which the r.m.s. value of the temperature fluctuation, T_{rms}, reaches the maximum (figure 7*b*). Furthermore, the Re number also reaches a maximum here as discussed in § 4.1. Together these results indicate that the decrease in T_{rms} and flow velocity are both caused by the transition to a 3-D flow regime and that the transition can be organized by Ra/Q.

https://doi.org/10.1017/jfm.2020.1047 Published online by Cambridge University Press

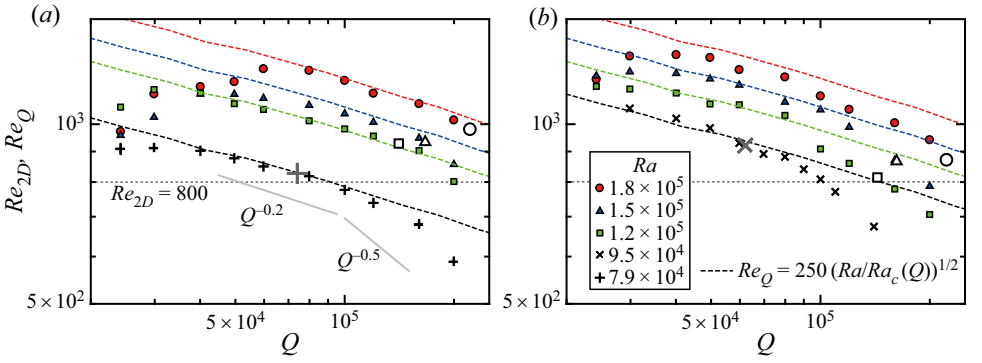

Figure 16. Variations in Reynolds numbers for quasi-2-D flows, Re_{2D}, plotted with decreasing Q at different Ra values and different number of rolls: (*a*) $n = 5$ and (*b*) $n = 6$, respectively. The grey lines are guides for variations proportional to $Q^{-0.2}$ and $Q^{-0.5}$; larger open symbols (grey cross symbols) indicate Re_{2D} values corresponding to Q_{OS} in figure 6. Coloured broken lines indicate approximations of the variations of Re_{2D} considering the influence of Q on the critical Ra at the onset of convection, $Ra_c(Q)$. The constant 250 is set empirically.

4. Discussion

The experimental and numerical results shown in the previous section indicate that the 2-D oscillatory convection accompanies oscillations of the recirculation vortex pairs situated between the main rolls, and that there are two different types of oscillations. The recirculation vortices play an important role in the onset of instabilities, which is deduced to be dominated by the inertia of the flow from the knowledge of absolute instability of the wake. Here we discuss the physics behind the variations in the Re number of quasi-2-D flows and its relation to the fraction of Q/Ra with arguments based on MHD for a unified understanding of the involved phenomena.

4.1. *Variation of the Reynolds number*

In the case of quasi-2-D convection consisting of parallel convection rolls, we use the velocity in the rolls, $U_{y,max}$, and the vessel height, L, to define the Reynolds number as $Re_{2D} = U_{y,max}L/\nu$. The variation of Re_{2D} with Q obtained at different Ra values for the five- and six-roll states are plotted in figure 16(*a*,*b*), respectively. Larger open symbols (and grey crosses) indicate Re_{2D} values corresponding to the critical value of the Chandrasekhar number for the onset of the oscillations Q_{OS} shown in figure 6; Q_{OS} here indicates the onset of more dynamic 2-D oscillations discussed in § 3.4 and is determined along the criteria mentioned in § 3.2. For the range of Ra numbers considered here, the oscillations occur for $Re_{2D} > 800$. It can be assumed that the flow velocities in the main convection rolls are sufficiently large in this range to entrain the vorticity from the recirculation vortex pair to form dynamic 2-D oscillations. A re-examination of data published in our previous papers (Tasaka *et al.* 2016; Vogt *et al.* 2018) also indicates that for $Q > 10^3$ the steady conditions maintain $Re_{2D} < 800$ and the first oscillation of five or six rolls appears at $Re_{2D} > 800$. Here, the value 800 of the Re number itself probably has no universal character and may change depending on the vessel aspect ratio, as discussed later.

The log–log plot in figure 16 indicates that the main part of the dependence of Re on Q cannot be described by a single power law as shown by the grey auxiliary lines in the figure representing the slopes of $Re_{2D} \propto Q^{-0.2}$ and $\propto Q^{-0.5}$; the variations seem to be steeper with respect to Q. Notably, there is a maximum in the Re number as in the temperature

https://doi.org/10.1017/jfm.2020.1047 Published online by Cambridge University Press

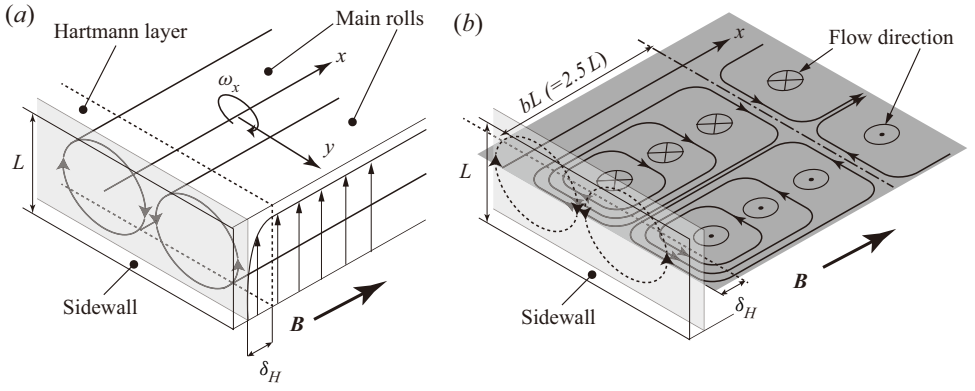

Figure 17. Schematic drawing of the Hartmann layer formed near a sidewall parallel to the magnetic field: (*a*) with convection rolls and (*b*) with contours of the induced electric currents displayed on the midplane.

fluctuations (figure 7), especially in the case of large Ra. The reduction of Re_{2D} in the case of small Q may be accompanied by the transition to a 3-D flow regime, whereas the decrease in flow amplitude at high Q may be due to the Hartmann braking effect.

4.2. *Scaling for variations of Reynolds numbers*

Here we consider the scaling law of Re_{2D} to cover a wide range of the variations shown in figure 16. To describe the variation in Re_{2D} where the slope gradually changes with Q, we express the effect of magnetic damping using the critical Rayleigh number for the onset of convection as a function of Q. The key phenomenon to evaluate the magnetic damping is the Hartmann braking in the boundary layer formed on the walls perpendicular to the magnetic field (Hartmann layer, figure 17). Burr & Müller (2002) explained Hartmann braking in the present system as follows:

In the core region the Lorenz forces are directed opposite to the convective motions whereas at the Hartmann walls their direction is reversed and the fluid is accelerated. This renders the Hartmann layers very thin and thereby, together with conducting Hartmann walls, they govern the current density and with it the damping of velocity in the core region. The energy removed from the core region is dissipated by Joule dissipation in the Hartmann walls and by Joule and viscous dissipation in the Hartmann layers.

In the present system, an electrically insulating material is used as the sidewalls and thus the energy dissipation occurs in the Hartmann layer. With increasing Q, the Hartmann layer becomes thinner and viscous dissipation becomes stronger. In the results of linear stability analysis performed by Burr & Müller (2002), the critical Ra number for the onset of convection with regard to Hartmann braking, $Ra_c(Q)$, was given as a relation of Ra_c versus $1/\tau_m$ (figure 18). The time scale of magnetic damping by the Hartmann braking, τ_m, is given from (22) in Burr & Müller (2002) as

$$\frac{1}{\tau_m} = \frac{Q^{1/2}}{b} + \frac{Qc_H}{b + c_H}, \tag{4.1}$$

where b and c_H denote the dimensionless half-width of the fluid layer parallel to the magnetic field and the electrical conductivity of the sidewall, respectively.

The Prandtl free-fall velocity for thermal convection indicates that the representative velocity W_0 is $W_0 \sim \sqrt{g\beta\Delta TL}$. This makes the Re number for the case of non-magnetic

https://doi.org/10.1017/jfm.2020.1047 Published online by Cambridge University Press

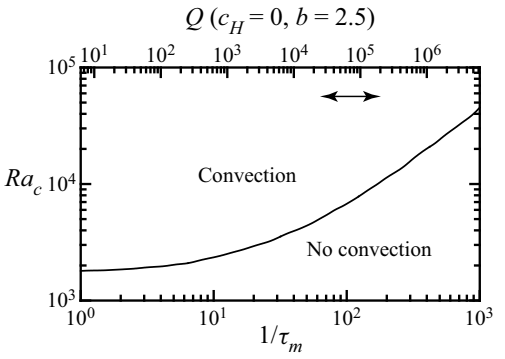

Figure 18. Neutral stability curve for the onset of convection replotted from Burr & Müller (2002). The top axis represents the corresponding Chandrasekhar number Q for $c_H = 0$ and $b = 2.5$ calculated from magnetic damping time τ_m in (22) of Burr & Müller (2002), where the arrow indicates the range of Q examined in the present study.

field approximately $Re \sim (Ra/Pr)^{1/2}$. By extending this relation, the variations in Re number can be expressed as

$$Re_Q \sim \left[\frac{Ra}{Pr}\frac{Ra_c(Q=0)}{Ra_c(Q)}\right]^{1/2} = A\left[\frac{Ra}{Ra_c(Q)}\right]^{1/2} \quad \text{(with } A \text{ a coefficient constant)}, \tag{4.2}$$

where the inertia generated by buoyancy is given as a value of Ra relative to $Ra_c(Q)$. We revisit figure 16 to evaluate the applicability of the present scaling law derived above. The dimensionless half-length is $b = 2.5$ and the sidewalls are electrically insulated ($c_H = 0$). The Ra_c–Q dataset was formed (figure 18) by reading off Ra_c–$1/\tau_m$ in Burr & Müller (2002). Variations of Re_Q are thus calculated from the dataset at different Ra numbers, as shown by dashed lines in figure 16, where the coefficient $A = 250$ was empirically determined to fit the result for the five-roll state ($n = 5$) at $Ra = 7.9 \times 10^4$. This value is very close to $[Ra_c(Q = 0)/Pr]^{1/2} = (1708/0.03)^{1/2} \approx 239$ in (4.2). The variations of Re_{2D} can be approximated by the present scaling law of (4.2) in the moderate Q range depending on Ra. This suggests that the convection velocity is determined by the effective Ra numbers, i.e. distance from the neutral stability curve under a horizontal magnetic field. The critical Chandrasekhar numbers, Q_{OS}, for the onset of 2-D oscillations appear to occur at which the present Re_{2D} data fail to match the present scaling law for large Q. The data also deviate from the scaling law for small Q, which arises from the transition to a 3-D flow regime discussed in the previous section.

4.3. *Scaling in the steady 2-D regime*

Variations in Re_{2D} appear steeper and detach from the scaling law of (4.2) for relatively large Q values (figure 16). At sufficiently large Q, 2-D oscillatory convection may be suppressed into steady 2-D convection. The scaling law describing the steeper slope may thus be derived to consider the condition. The influence of viscous dissipation can be disregarded in cases of sufficiently large Ra and Q, and the equation of motion for the vertical velocity w in the quasi-2-D flows is reduced to

$$\frac{Dw}{Dt} \sim F_b - F_H, \tag{4.3}$$

https://doi.org/10.1017/jfm.2020.1047 Published online by Cambridge University Press

where D/Dt is a material derivative, and the force terms on the right-hand side are the buoyancy and the magnetic damping by Hartmann braking. The order of (4.3) is evaluated using the characteristic velocity W with the time scale of Hartmann braking τ_H as

$$\frac{\mathrm{D}W}{\mathrm{D}t} \sim g\beta\Delta T - \frac{W}{\tau_H}. \tag{4.4}$$

From Sommeria & Moreau (1982), the dissipation time scale of the Hartmann braking is given as $\tau_H = (a/2B)(\rho/\sigma\nu)^{1/2}$ with the spacing between walls a. The expression of τ_H is equivalent to τ_m in (4.1) for $c_H = 0$. Here we reformulate the time scale using length scale L as

$$\frac{1}{\tau_H} \sim \frac{Q^{1/2}}{b}\frac{\nu}{L^2}. \tag{4.5}$$

This includes the dimensionless half-width b (= 2.5), whereas the thickness of the Hartmann layer,

$$\delta_H \sim Q^{-1/2}L, \tag{4.6}$$

is independent of b.

It is assumed that the fluid flow is in steady condition with Q larger than the critical Chandrasekhar number $Q_{OS}(Ra)$ for the onset of 2-D oscillations. Equilibrium velocity W^* in the condition is thus determined by the balance between the buoyancy and the magnetic damping by Hartmann braking. Following the procedure to evaluate convection velocity considering magnetic damping in Davidson (2017, § 6.2.5), (4.4) is simplified by substituting (4.5):

$$\left.\begin{aligned} g\beta\Delta T &= \frac{W^*}{\tau_H}, \\ Ra\frac{\kappa\nu}{L^3} &= W^*\frac{Q^{1/2}}{b}\frac{\nu}{L^2}, \\ W^* &= \frac{Ra}{Q^{1/2}}\frac{\kappa}{L}b. \end{aligned}\right\} \tag{4.7}$$

The Re number for steady quasi-2-D flows becomes

$$Re_{2D} = \frac{W^*L}{\nu} \sim \frac{Ra}{Q^{1/2}}\frac{b}{Pr}. \tag{4.8}$$

Equation (4.8) indicates that the variations in Re_{2D} depend on Q with an exponent of $-1/2$ for the limiting case that inertia can be neglected compared with the electromagnetic forces, here $Q > 10^5$ in figure 16. Using Prandtl free-fall theory for a non-magnetic field, $Re \sim (Ra/Pr)^{1/2}$, the relative Re number under magnetic field to this Re becomes

$$\frac{Re_{2D}}{Re} \sim \left(\frac{Ra}{Q}\right)^{1/2}\frac{b}{Pr^{1/2}}. \tag{4.9}$$

Variations in Re_{2D} reduced by $Ra^{1/2}$ are shown in figure 19, where Q in the abscissa is also reduced by Ra. The curve representing the power law derived above is indicated by a broken line. The data collapse reasonably well into a unified curve and the variations of Re seem to approach the slope of the broken line for larger Q, $Q/Ra \gtrsim 1$. It can be speculated that, if Q/Ra values decrease, the data deviate from this power law after the

https://doi.org/10.1017/jfm.2020.1047 Published online by Cambridge University Press

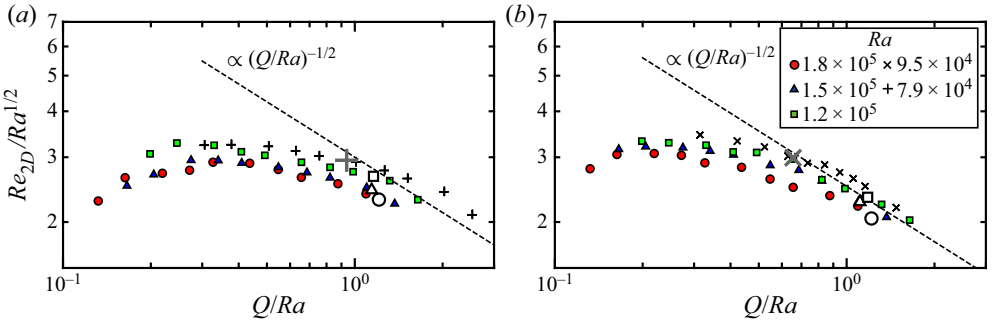

Figure 19. Values of Re_{2D} as a function of Q/Ra for different Ra conditions reduced by $Ra^{0.5}$ according to the scaling law: (*a*) $n = 5$ and (*b*) $n = 6$. Larger open symbols (grey cross symbols) indicate Re_{2D} values corresponding to Q_{OS} in figure 6.

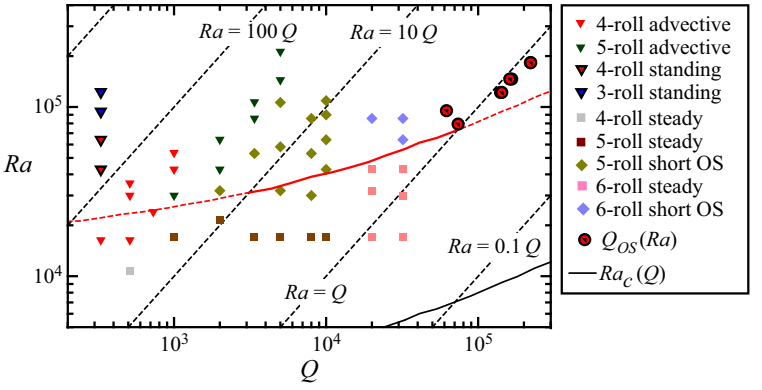

Figure 20. Critical Chandrasekhar number Q_{OS} for different Ra values (figure 6) plotted on the regime diagram provided by Vogt *et al.* (2018), where broken black lines indicate contours of Ra/Q. The solid black line shows critical Rayleigh numbers for the onset of convection calculated from the results of Burr & Müller (2002) with $b = 2.5$. The red line represents the contour line of $Re_Q = 250[Ra/Ra_c(Q)]^{1/2} = 800$ as the proposed critical condition of quasi-2-D oscillations for cases of $Q/Ra \lesssim 1$.

2-D oscillations have appeared. The power law based on the assumption of the balance between the buoyancy and the magnetic damping by Hartmann braking is not valid at weaker magnetic fields where inertia must be taken into account.

The applicability of the criterion that the present power law of Re_Q determines the onset of 2-D oscillation is now evaluated for the previous results obtained with $Q/Ra < 1$. The regime diagram summarized in Vogt *et al.* (2018) is shown in figure 20 with the critical Chandrasekhar number Q_{OS} obtained in this study, where square and diamond symbols indicate the steady and the 2-D oscillation regimes with five or six rolls, respectively. The red line in figure 20 represents the contour $Re_Q = 250[Ra/Ra_c(Q)]^{1/2} = 800$, where $Re_{2D} = 800$ is chosen as the lower limit at which the 2-D oscillation emerges (figure 16). The line is a good approximation of the border between the steady and the 2-D oscillation regimes.

Through a detailed investigation of the results obtained here and following the above discussion, the flow regimes may be dominated by a Re number determined by the distance from the neutral stability curve (black solid line in figures 18 and 20). The fraction Q/Ra appears as the dominant factor that determines the regimes in conjunction with Re, e.g.

https://doi.org/10.1017/jfm.2020.1047 Published online by Cambridge University Press

$Q/Ra \approx 1$ for the onset of dynamic oscillation, and $Q/Ra \approx 0.3$ for the transition to a 3-D flow regime. These conditions of the fraction, however, are given for the specific value of b ($= 2.5$). It is thus trivial that the fraction may not be a universal factor to describe the phenomena, and the condition $Q/Ra \approx 1$ for the onset of dynamic oscillation is modified by different b values.

4.4. *Relation to previous studies*

According to the derivation process of the scaling law in (4.9), the Re number strongly depends on the half-length of the fluid layer (b in (4.9)) in the direction of the magnetic field because of the dominance of Hartmann braking on the fluid layer. The fluid layer used in Burr & Müller (2002) has a larger $b = 5$, compared with $b = 2.5$ in the present set-up (figure 17). The differences in the critical conditions for the onset of oscillatory convection in their results show substantially smaller critical Ra numbers than the present results, which can be explained by a further discussion of reasons below. Here we assume that the flow regimes are dominated by the Re number according to the previous discussions. Fluid layers of larger horizontal extents in the direction of the magnetic field would achieve sufficiently large Re numbers for the transitions even with smaller Ra, at similar Q conditions to those in the present study. This is because of the reduced influence of Hartmann braking on the variations of Re. There are also differences in the criterion determining the onset of oscillation. Burr & Müller (2002) used the temperature fluctuation intensity measured at the central part of the fluid layer, whereas we determined the investigated frequency component $f = f_{OS}$ of the velocity fluctuations at which the r.m.s. value reaches the local maximum in the profile. As mentioned in § 3.4, there are two different types of 2-D oscillatory convection: weak and local oscillations of the recirculation vortex pair between the main rolls, and more dynamic and global elliptic oscillations of the main rolls accompanying vorticity entrainment from the recirculation vortex pair. From these observations it is suggested that Burr & Müller (2002) detected the former, whereas the present study investigated the latter.

The flow development and transitions dominated by Hartmann braking are not a specific problem in this study, but are common characteristics that influence low-magnetic-Reynolds-number flows confined by walls of electrically insulating materials. Knaepen & Moreau (2008) predicted that MHD damping in the flows confined by walls perpendicular to the magnetic field is not characterized by the interaction parameter $N = Q/Re$, but by Ha/Re (or N/Ha in a different form; see also Sommeria & Moreau (1982) and Moreau, Thess & Tsinober (2007)). In the present system, Ha/Re is modified to $(QPr/Ra)^{1/2}$ as $Re \propto (Ra/Pr)^{1/2}$. This prediction agrees with the results obtained here. It may thus be concluded that the present results provide experimental evidence for this prediction.

5. Concluding remarks

We investigated 2-D oscillatory motions on quasi-2-D convection rolls that have been reported in Rayleigh–Bénard convection with an imposed horizontal magnetic field at relatively large Rayleigh-number Ra and Chandrasekhar-number Q conditions. The investigation was performed by considering the morphology, generation and mechanism that give rise to the oscillations through laboratory experiments using eutectic GaInSn as the test fluid filling in a vessel with an aspect ratio of five. Supplemental numerical simulations were performed to determine the details of the flow structures. Multi-line measurements of the instantaneous velocity profiles performed by ultrasonic

https://doi.org/10.1017/jfm.2020.1047 Published online by Cambridge University Press

velocity profiling at conditions of $7.9 \times 10^4 \leq Ra \leq 1.8 \times 10^5$ and $2.5 \times 10^4 \leq Q \leq 1.9 \times 10^5$ and the numerical simulations elucidated the emergence of two different types of 2-D oscillations. One is dynamic and global oscillations accompanied by vorticity entrainment from recirculation vortex pairing of separation flows detaching from the walls between neighbouring main rolls. The other is weak localized oscillations of the vortex pair. The source of the oscillations was found to lie in the periodic oscillations of the recirculation vortex pair. Despite different Ra conditions, the oscillations occur at similar Reynolds numbers ($Re_{2D} > 800$). These Re_{2D} values are sufficiently large to cause oscillatory instability in the recirculation vortex pairs. This is considerably different from the 3-D travelling wave propagation along the roll axis predicted by stability analysis at relatively small Q conditions, $Q = O(10)$, as enlargements of the Busse balloon. The 2-D oscillations are caused by sufficiently high inertia provided by the large Ra and 2-D restrictions. The intensity of the temperature fluctuations and Reynolds number Re_{2D} increase with decreasing Q, along with the development of 2-D oscillations, and further decrease with decreasing Q because of a transition from the 2-D oscillation regime to a 3-D flow regime.

A scaling law describing the variation of Re_{2D} was derived with an effective Ra number reduced by a critical Ra number as a function of Q as $Re_Q \propto [Ra/Ra_c(Q)]^{1/2}$. The contour of $Re_Q = 800$ given from the scaling law shows good agreement with the boundaries of oscillatory and steady-state regimes obtained in previous experiments under relatively small Q conditions. A considerably steeper decrease of Re_{2D} around the onset of the 2-D oscillations for relatively large Q seems to approach $(Q/Ra)^{-1/2}$. This corresponds to the scaling law derived from the assumption of a balance between buoyancy and magnetic damping by Hartmann braking near the sidewall of the vessel perpendicular to the magnetic field in the steady regime. These results suggest that the emergence of 2-D oscillatory convection is governed by the competition between the buoyancy in the core region and viscous dissipation in the thin Hartmann layer, and therefore its onset is determined by Re_{2D}.

Supplementary movies. Supplementary movies are available at https://doi.org/10.1017/jfm.2020.1047.

Acknowledgements. Numerical simulations were performed on the Earth Simulator at JAMSTEC.

Funding. This work was supported by JSPS KAKENHI grant no. 24244073. The activities of Y.T. at Helmholtz Zentrum Dresden-Rossendorf (HZDR) were supported by JSPS KAKENHI grant no. 15KK01219. The authors acknowledge Dr S. Eckert and Dr T. Vogt in HZDR for their technical support in the experiments and fruitful discussions.

Declaration of interests. The authors report no conflict of interest.

Author ORCIDs.
Y. Tasaka https://orcid.org/0000-0002-8943-4803;
T. Yanagisawa https://orcid.org/0000-0001-6289-938X;
T. Miyagoshi https://orcid.org/0000-0002-8908-9990.

References

Ahlers, G., Grossmann, S. & Lohse, D. 2009 Heat transfer and large scale dynamics in turbulent Rayleigh–Bénard convection. *Rev. Mod. Phys.* **81**, 503–537.

Bodenschatz, E., Pesch, W. & Ahlers, G. 2000 Recent developments in Rayleigh–Bénard convection. *Annu. Rev. Fluid Mech.* **32**, 709–778.

Burr, U. & Müller, U. 2002 Rayleigh–Bénard convection in liquid metal layers under the influence of a horizontal magnetic field. *J. Fluid Mech.* **453**, 345–369.

https://doi.org/10.1017/jfm.2020.1047 Published online by Cambridge University Press

BUSSE, F.H. 1978 Non-linear properties of thermal convection. *Rep. Prog. Phys.* **41**, 1929–1967.
BUSSE, F.H. & CLEVER, R.M. 1983 Stability of convection rolls in the presence of a horizontal magnetic field. *J. Méc. Théor. Appl.* **2**, 495–502.
CHANDRASEKHAR, S. 1961 *Hydrodynamic and Hydromagnetic Stability*. Oxford University Press.
CLEVER, R.M. & BUSSE, F.H. 1987 Nonlinear oscillatory convection. *J. Fluid Mech.* **176**, 403–417.
DAVIDSON, P.A. 1995 Magnetic damping of jets and vortices. *J. Fluid Mech.* **299**, 153–186.
DAVIDSON, P.A. 2017 *Introduction to Magnetohydrodynamics*, 2nd edn. Cambridge University Press.
DRAZIN, P.G. & REID, W.H. 1998 *Hydrodynamic Stability*. Cambridge University Press.
ECKERT, S., CRAMER, A. & GERBETH, G. 2007 Velocity measurement techniques for liquid metal flows. In *Magnetohydrodynamics* (ed. S. Molokov, R. Moreau & H.K. Moffatt), pp. 275–294. Springer.
KNAEPEN, B. & MOREAU, R. 2008 Magnetohydrodynamic turbulence at low magnetic Reynolds number. *Annu. Rev. Fluid Mech.* **4**, 25–45.
KOSCHMIEDER, E.L. 1993 *Bénard Cells and Taylor Vortices*. Cambridge University Press.
KRISHNAMURTI, R. & HOWARD, L.N. 1981 Large-scale flow generation in turbulent convection. *Proc. Natl Acad. Sci. USA* **78**, 1981–1985.
LAPPA, M. 2010 *Thermal Convection: Patters, Evolution and Stability*. Wiley.
LOHSE, D. & XIA, K.-Q. 2010 Small-scale properties of turbulent Rayleigh–Bénard convection. *Annu. Rev. Fluid Mech.* **42**, 335–364.
MASHIKO, T., TSUJI, Y., MIZUNO, T. & SANO, M. 2004 Instantaneous measurement of velocity fields in developed thermal turbulence in mercury. *Phys. Rev.* E **69**, 036306.
MOREAU, R., THESS, A. & TSINOBER, A. 2007 MHD turbulence at low magnetic Reynolds number: present understanding and future needs. In *Magnetohydrodynamics* (ed. S. Molokov, R. Moreau & H.K. Moffatt), pp. 231–246. Springer.
MORLEY, N.B., BURRIS, J., CADWALLADER, L.C. & NORNBERG, M.D. 2008 GaInSn usage in the research laboratory. *Rev. Sci. Instrum.* **79**, 056107.
PLEVACHUK, Y., SKLYARCHUK, V., ECKERT, S., GERBETH, G. & NOVAKOVIC, R. 2014 Thermophysical properties of the liquid Ga-In-Sn eutectic alloy. *J. Chem. Engng Data* **59**, 757–763.
SOMMERIA, J. & MOREAU, R. 1982 Why, how, and when, MHD turbulence becomes two-dimensional. *J. Fluid Mech.* **118**, 507–518.
TAKEDA, Y. 2012 *Ultrasonic doppler velocity profiler for fluid flow*. Fluid Mechanics and Its Applications, vol. 101. Springer Science & Business Media.
TASAKA, Y., IGAKI, K., YANAGISAWA, T., VOGT, T., ZUERNER, T. & ECKERT, S. 2016 Regular flow reversals in Rayleigh–Bénard convection in a horizontal magnetic field. *Phys. Rev.* E **93**, 043109.
TSUJI, Y., MIZUNO, T., MASHIKO, T. & SANO, M. 2005 Mean wind in convective turbulence of mercury. *Phys. Rev. Lett.* **94**, 034501.
VOGT, T., ISHIMI, W., YANAGISAWA, T., TASAKA, Y., SAKURABA, A. & ECKERT, S. 2018 Transition between quasi-two-dimensional and three-dimensional Rayleigh–Bénard convection in a horizontal magnetic field. *Phys. Rev. Fluids* **3**, 013503.
YANAGISAWA, T., HAMANO, Y., MIYAGOSHI, T., YAMAGISHI, Y., TASAKA, Y. & TAKEDA, Y. 2013 Convection patterns in a liquid metal under an imposed horizontal magnetic field. *Phys. Rev.* E **88**, 063020.
YANAGISAWA, T., HAMANO, Y. & SAKURABA, A. 2015 Flow reversals in low-Prandtl-number Rayleigh–Bénard convection controlled by horizontal circulations. *Phys. Rev.* E **92**, 023018.
YANAGISAWA, T., YAMAGISHI, Y., HAMANO, Y., TASAKA, Y. & TAKEDA, Y. 2011 Spontaneous flow reversals in Rayleigh–Bénard convection of a liquid gallium. *Phys. Rev.* E **83**, 036307.
YANAGISAWA, T., YAMAGISHI, Y., HAMANO, Y., TASAKA, Y., YOSHIDA, M., YANO, K. & TAKEDA, Y. 2010 Structure of large-scale flows and their oscillation in the thermal convection of liquid metal. *Phys. Rev.* E **82**, 016320.

https://doi.org/10.1017/jfm.2020.1047 Published online by Cambridge University Press